Corrected 17 February 2021; see below

science.sciencemag.org/content/371/6527/eabc3393/suppl/DC1

Supplementary Materials for

JARID2 and AEBP2 regulate PRC2 in the presence of H2AK119ub1 and other histone modifications

Vignesh Kasinath*, Curtis Beck, Paul Sauer, Simon Poepsel, Jennifer Kosmatka, Marco Faini, Daniel Toso, Ruedi Aebersold, Eva Nogales*

*Corresponding author. Email: enogales@lbl.gov (E.N.); vigneshk@berkeley.edu (V.K.)

Published 22 January 2021, *Science* **371**, eabc3393 (2021)
DOI: 10.1126/science.abc3393

This PDF file includes:

Other Supplementary Material for this manuscript includes the following:
(available at science.sciencemag.org/content/371/6527/eabc3393/suppl/DC1)

MDAR Reproducibility Checklist (.pdf)
Movie S1 (.mp4)

Correction: In the originally published version of this Research Article, the authors inadvertently omitted a key reference [E. J. Ge *et al.*, *J. Am. Chem. Soc.* **141**, 15029–15039 (2019)]. In the updated file, this reference was added to the reference list as reference 32, and the references originally numbered 32 to 58 were renumbered accordingly as 33 to 59. The two in-text citations in the supplementary materials have been updated to reflect the new numbering of the references, and the reference list has been corrected. The text itself was not otherwise changed.

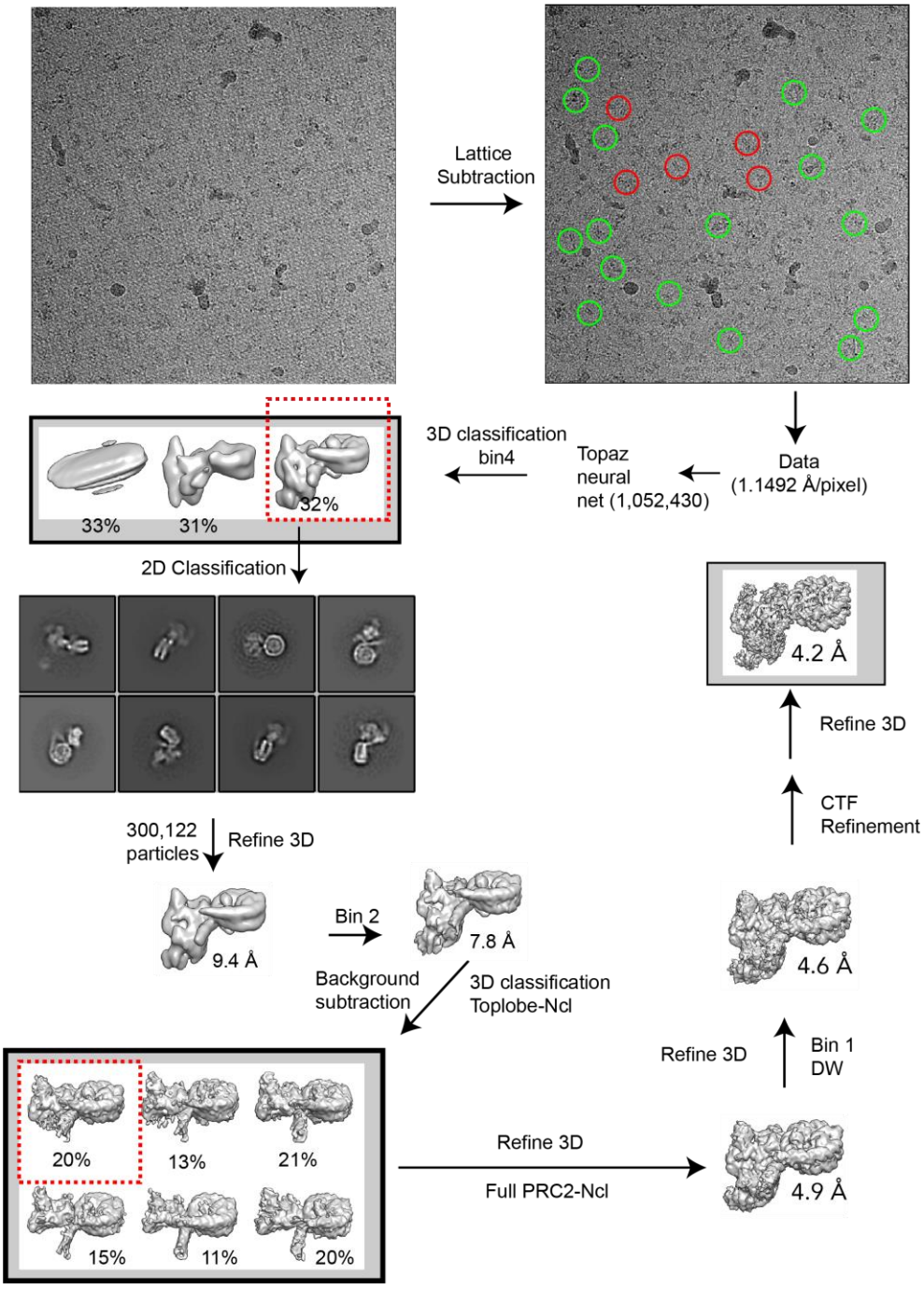

Fig. S1. Processing work flow for PRC2-AEBP2-JARID2 (1-450) bound to H2AK119ub containing mono-nucleosome collected on a Titan Krios with a Gatan K2 detector. Red circles represent manually picked particles for topaz training and green circles represent topaz picked particles after neural net training (only a subset is shown for clarity).

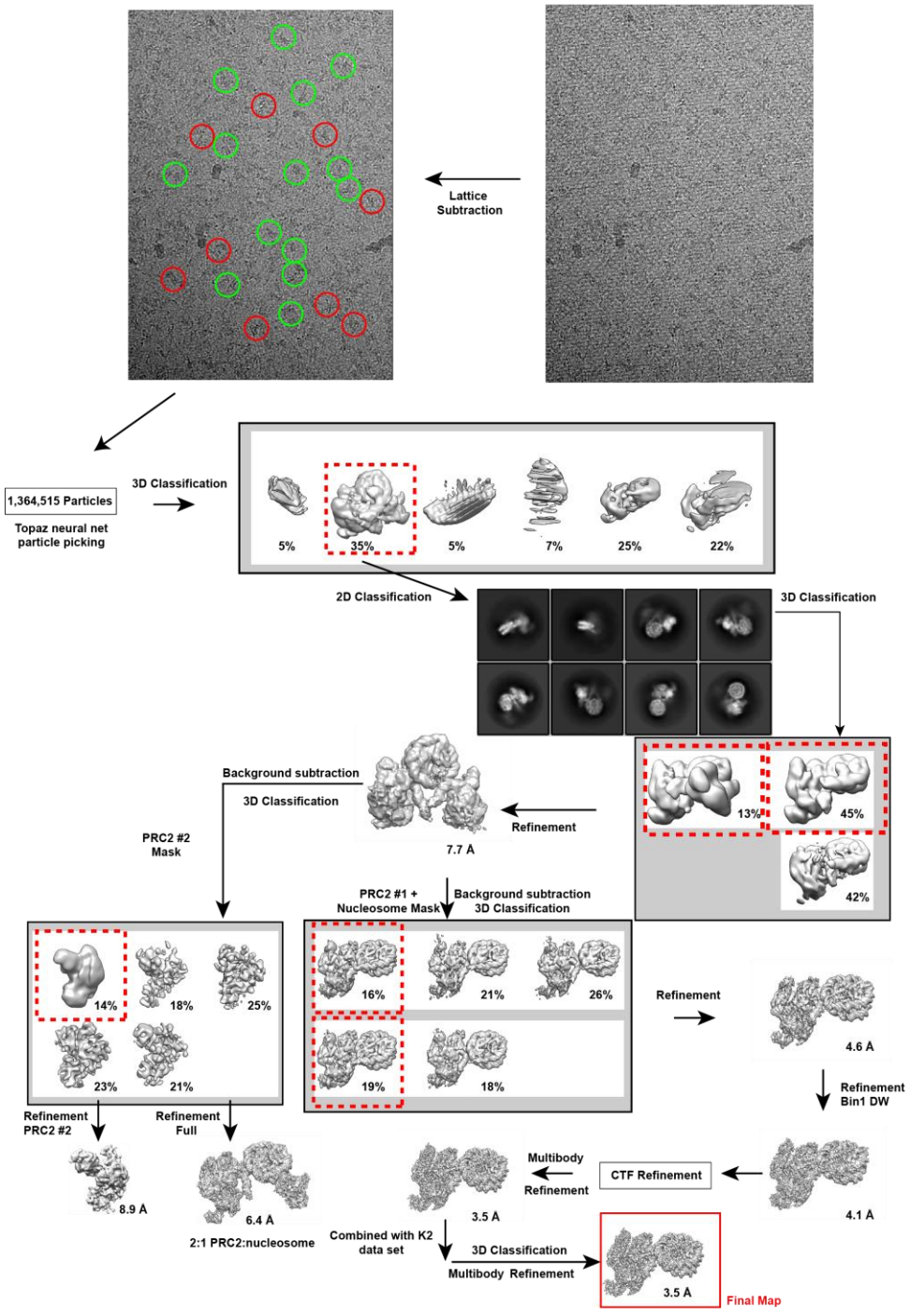

Fig. S2. Processing work flow for PRC2-AEBP2-JARID2 (aa 1-450) bound to H2AK119ub containing mono-nucleosome collected on a Titan Krios with Gatan K3 camera. Red circles represent manually picked particles for topaz training and green circles represent topaz picked particles after neural net training (only a subset is shown for clarity).

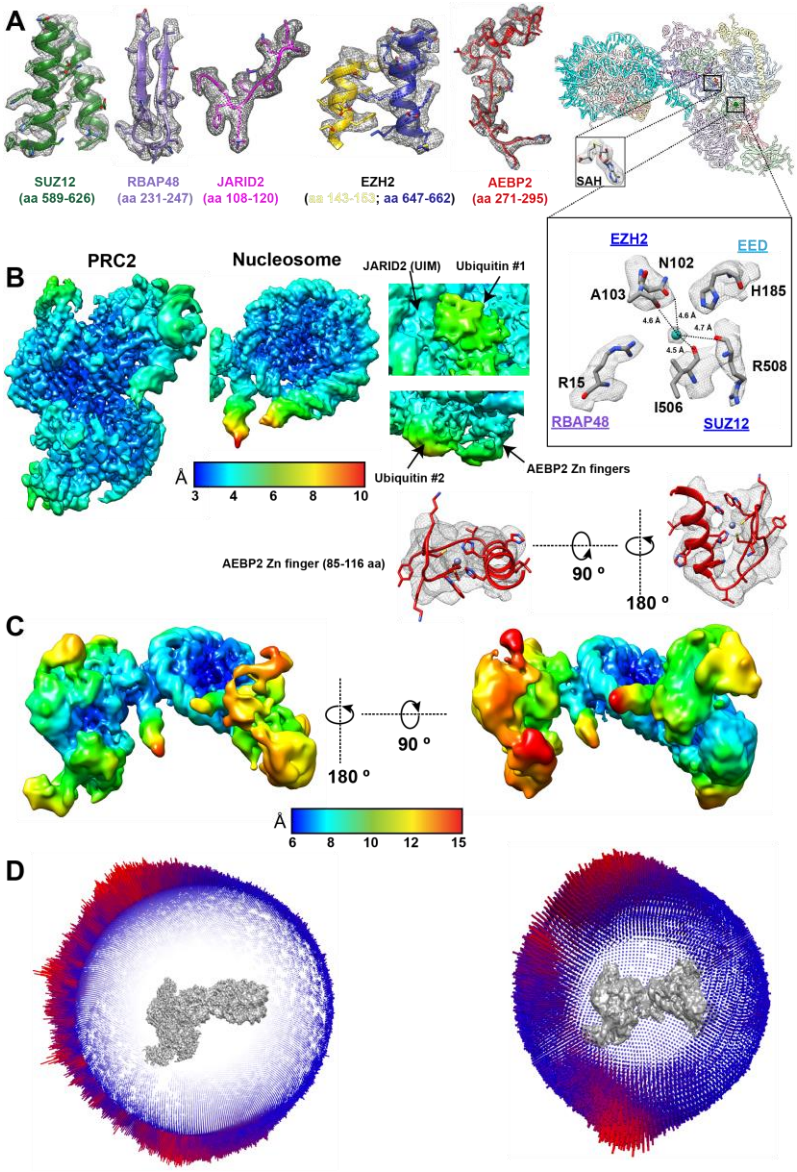

Fig. S3. (A) Cryo-EM density (contour level: 0.024) and built in models for regions of the final map for PRC2-AEBP2-JARID2 (aa 1-450) bound to H2AK119ub1 containing mono-nucleosome (Ncl-ub) corresponding to the different proteins in PRC2. On the far right is the full model of PRC2-nucleosome with a close up view of two regions of PRC2, one showing the density for SAH and the corresponding atomic model of SAH and the other in the center of PRC2 showing density for a presumed divalent metal ion that appears to interact with regions from the four core subunits of PRC2 (EZH2, EED, SUZ12, and RBAP48). (B) Local resolution (Å) for PRC2 and for the nucleosome shown in high threshold and the close-up views of the local resolution of both ubiquitin molecules, JARID2 UIM and the AEBP2 tandem zinc fingers in lower threshold in the

final reconstructions. The cryo-EM density is shown as mesh and the fitted model for AEBP2 zinc-finger (85-116 aa) is shown in red. (C) Local resolution (Å) of the map containing two PRC2 bound to a nucleosome. (D) (Left) Euler angle distribution for the particles after the final refinement of 1:1 PRC2:Ncl-ub after combining the two data sets. (Right) Euler angle distribution for the particles after the final refinement of the 2:1 PRC2:Ncl-ub.

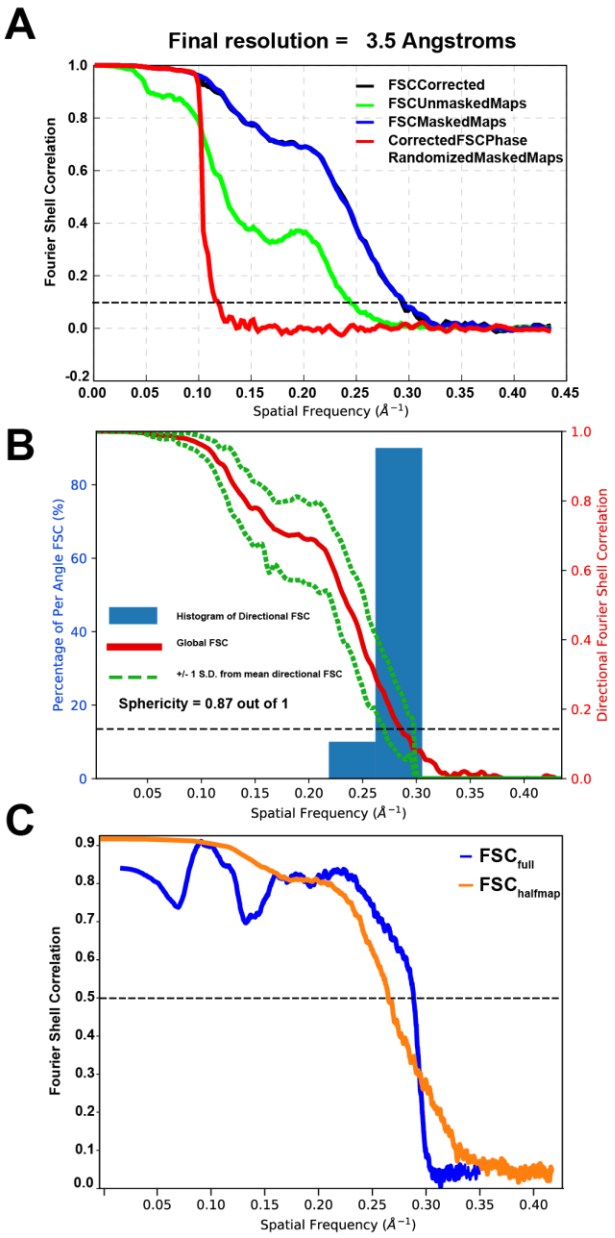

Fig. S4. (A) FSC curves for the final, refined model. (B) 3D FSC for final Phenix-refined model vs full map. (C) Model vs Map FSC for final Phenix-refined model versus full map (Blue) and half-maps (orange). FSC/3D FSC.

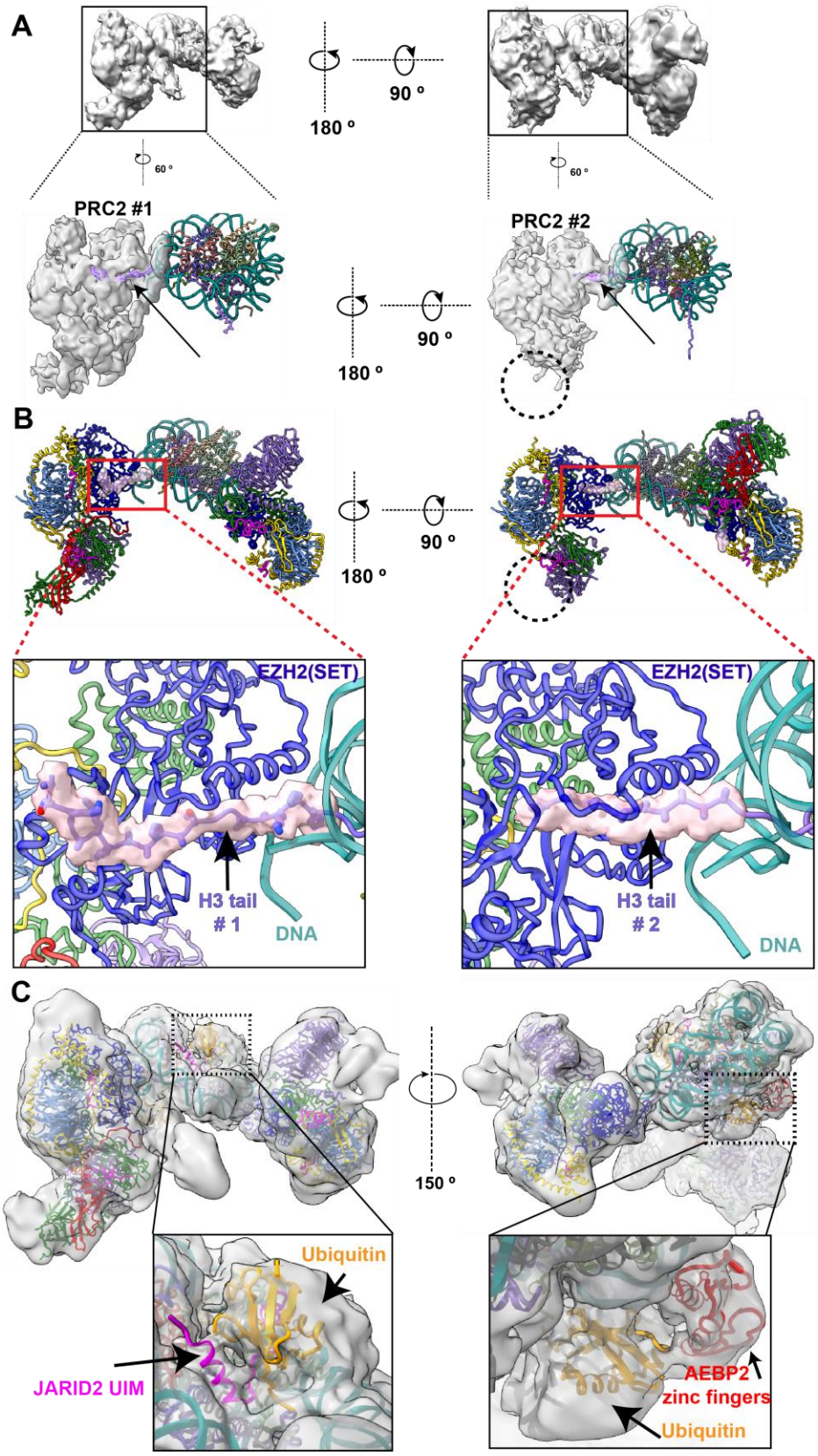
A
90 °
180 °
60 °
PRC2 #1
PRC2 #2
B
EZH2(SET)
H3 tail
1
DNA
EZH2(SET)
H3 tail
2
DNA
C
150 °
Ubiquitin
JARID2 UIM
AEBP2
zinc fingers
Ubiquitin

Fig. S5. (A) (Top) The cryo-EM reconstruction of two PRC2-AJ$_{1-450}$ engaging one each of the two histone H3 tails, on the opposite sides of the Ncl-Ub. (Bottom) The density map for each individual PRC2-ApJ$_{1-450}$ complex, with the atomic models of the nucleosome and the H3 tails (pink) docked into the density. (B) (Top) Full model of the two PRC2-AJ$_{1-450}$ engaging the nucleosome, with histone H3 density shown in pink. (Bottom) Close up view of the density for the histone H3 tails. Each PRC2 simultaneously interacts with one of the histone H3 tails (density shown in pink with model in stick representation). (C) Comparison of the cryo-EM density near each of the ubiquitins in the PRC2-sandwiched nucleosome, shown at low contour level (0.003). The clear differences in the density of the two regions allows to assign one to JARID2-ubiquitin and the other to AEBP2-ubiquitin (model docking show that the densities correspond well to that seen in the 1:1 PRC2-nucleosome complex).

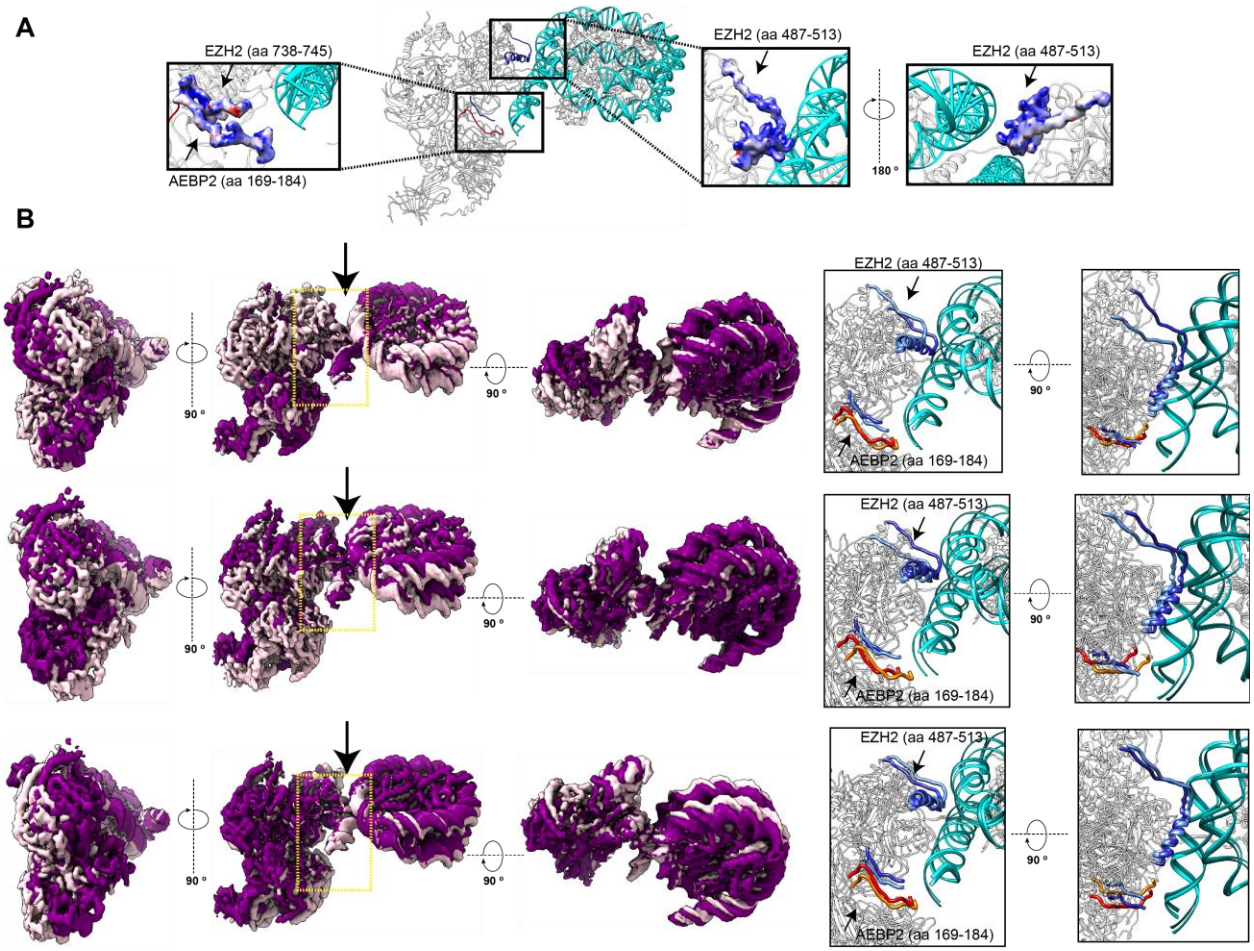

Fig. S6. (A) Close-up view at the electrostatic potential of the EZH2 bridge helix region (aa 487-513) and an AEBP2 segment rich in lysine and arginine (aa 169-184) that interact with DNA showing the presence of strong positively charged surfaces in both segments. (B) Conformational flexibility observed using multibody analysis in RELION(*43*) in which PRC2 and nucleosome were treated as independent bodies. The three rows depict, in three orthogonal orientations, the representative conformational variance for the first three eigenvectors (63%). They show that the interface of PRC2-nucleosome interaction (black arrow) is flexible. On the far right, shown in two orthogonal orientations, are corresponding close ups of the nucleosome interacting regions (corresponding to the yellow dashed box on the left). The EZH2 bridge helix (aa 487-513) and C-terminus (aa 738-745) are shown in dark blue/light blue, the AEBP2 lysine and arginine rich segment (aa 169-174) in red/orange, and the nucleosomal DNA, shown in dark cyan/cyan. The dark-to-light shades of the respective colors illustrate the range of movement of these regions.

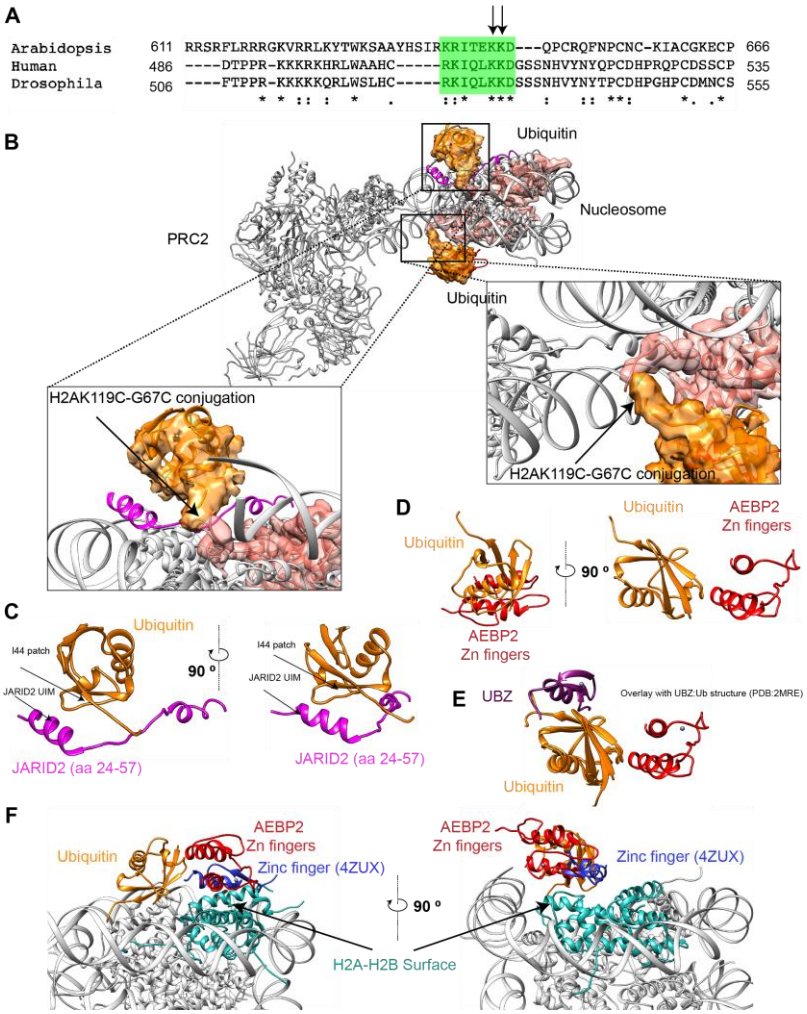

Fig. S7. (A) Amino acid sequence alignment of a part of EZH2 showing sequence conservation of the amino acids in the bridge helix involved in interaction with histone H3 tail, nucleosome DNA and EZH2 (SET) domain (highlighted in green). Auto-methylation lysines are indicated by black arrows. (B) Structure of PRC2-AJ$_{1\text{-}450}$ bound to Ncl-ub showing the cryo-EM density for ubiquitin (orange) and H2A (salmon) (filtered based on local resolution). Close-up view showing the structure of ubiquitin rigid-body docked into the density such that the C-terminal tail of ubiquitin containing G76C is ~ 3 Å from the H2AK119C. (C) Model of the JARID2 (aa 24-57) interaction with ubiquitin view in the same orientation as the close-up in (A), showing that I44-containing segment of ubiquitin is facing the JARID2 UIM. (D) Model of the ubiquitin-AEBP2 zinc finger interaction view in the same orientation as the close-up in (A) (left) and rotated 90 º (right). (E) Superposition of the model of ubiquitin-AEBP2 zinc finger from this study with the NMR structure of the ubiquitin binding zinc finger (purple) bound to ubiquitin (orange; PDB:2MRE(*58*)) illustrating that the AEBP2 zinc finger does not interact with the canonical ubiquitin surface. (E) Superposition of the model of the ubiquitin-AEBP2 zinc finger from this study with the zinc finger (blue) from SAGA DUB module bound to ubiquitinated nucleosome (PDB:4ZUX(29)) showing that they interact with the same H2A-H2B surface. The comparison was performed after rigid body docking the nucleosome in 6T9L within the cryo-EM density of PRC2-AJ$_{1\text{-}450}$ bound to Ncl-ub. Only the zinc finger from 6T9L is shown for clarity.

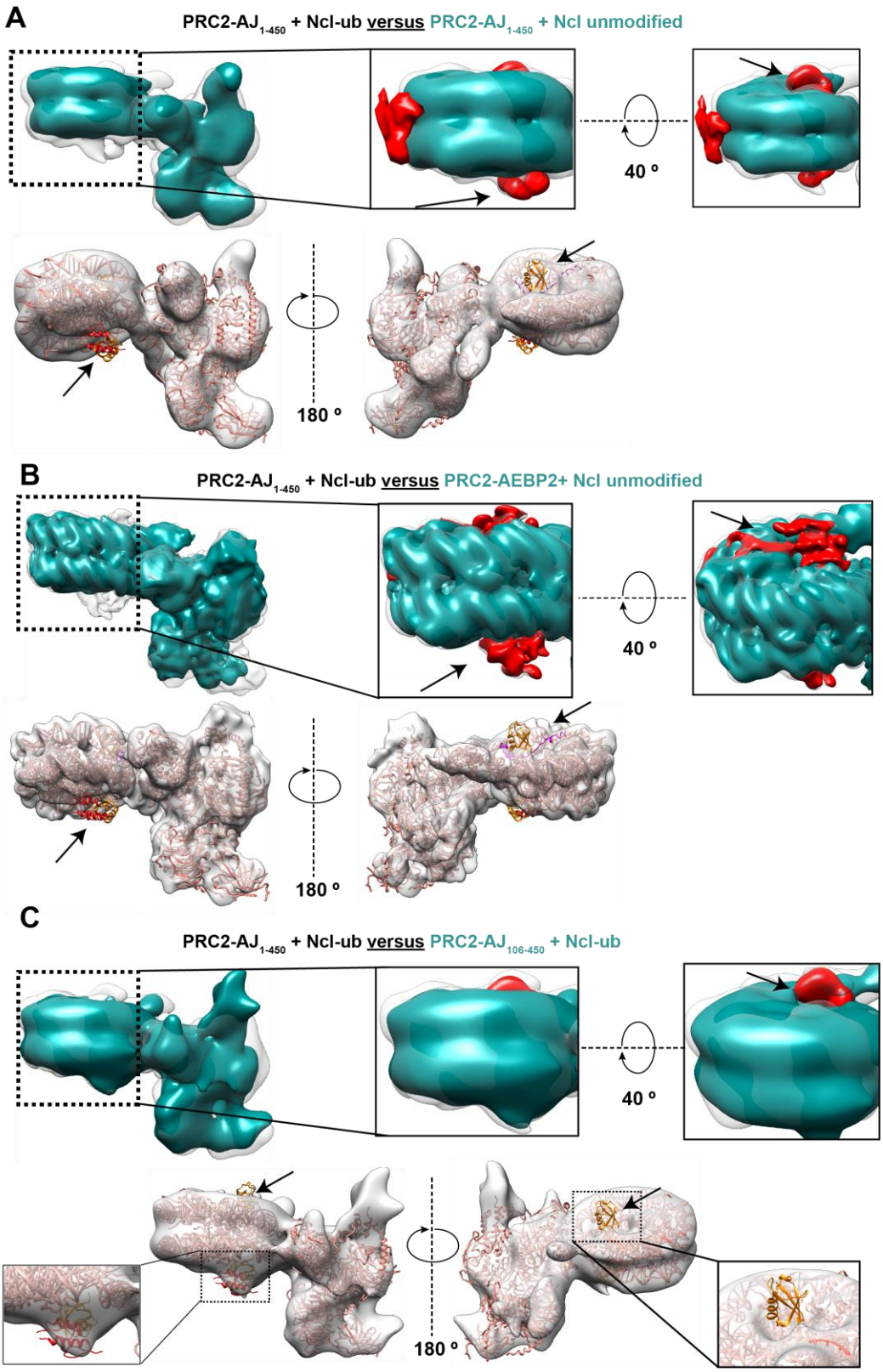
A
PRC2-AJ1-450 + Ncl-ub versus PRC2-AJ1-450 + Ncl unmodified
40 º
180 º
B
PRC2-AJ1-450 + Ncl-ub versus PRC2-AEBP2+ Ncl unmodified
40 º
180 º
C
PRC2-AJ1-450 + Ncl-ub versus PRC2-AJ106-450 + Ncl-ub
40 º
180 º

Fig. S8. (A) (Top) Overlay of PRC2-AJ$_{1-450}$ cryo-EM maps bound to a H2AK119ub-containing nucleosome (transparent map) and to an unmodified nucleosome (dark cyan). Close up views of the nucleosome with the difference map density for JARID2, AEBP2 zinc finger and ubiquitin are shown in red (indicated by black arrow). Both maps were lowpass filtered to 15 Å for comparison. (Bottom) Model of PRC2-AJ$_{1-450}$ bound to H2AK119ub-containing nucleosome docked into the cryo-EM map of PRC2-AJ$_{1-450}$ bound to unmodified nucleosome (transparent light grey) with arrows indicating ubiquitin, JARID2 and AEBP2 zinc finger for which no density is visible. (B) (Top) Overlay of PRC2-AJ$_{1-450}$ cryo-EM maps bound to a H2AK119ub-containing unmodified nucleosome (transparent map) and PRC2-AEBP2 bound to an unmodified nucleosome (dark cyan). Close up views of the nucleosome with the difference map density for AEBP2 zinc finger and ubiquitin shown in red (indicated by the black arrow). Both maps were lowpass filtered to 8 Å for comparison. (Bottom) Model of PRC2-AJ$_{1-450}$ bound to H2AK119ub-containing nucleosome docked into the cryo-EM map of PRC2-AEBP2 bound to an unmodified nucleosome (transparent light grey) with arrows indicating ubiquitin, JARID2 and AEBP2 zinc finger for which no density is visible. (C) (Top) Overlay of the cryo-EM reconstructions of PRC2-ApJ$_{106-450}$ bound to H2AK119ub nucleosome (dark cyan) with that of PRC2-AJ$_{1-450}$ bound to H2AK119ub containing nucleosome (transparent map). Close up views of the nucleosome with difference map density for the ubiquitin that binds JARID2 shown in red (indicated by black arrow). Both maps were filtered to 18 Å for comparison. (Bottom) Model of PRC2-AJ$_{1-450}$ bound to H2AK119ub-containing nucleosome docked into the cryo-EM map of PRC2-AJ$_{106-450}$ bound to a H2AK119ub unmodified nucleosome (transparent light grey) with arrows indicating ubiquitin and JARID2 for which no density is visible.

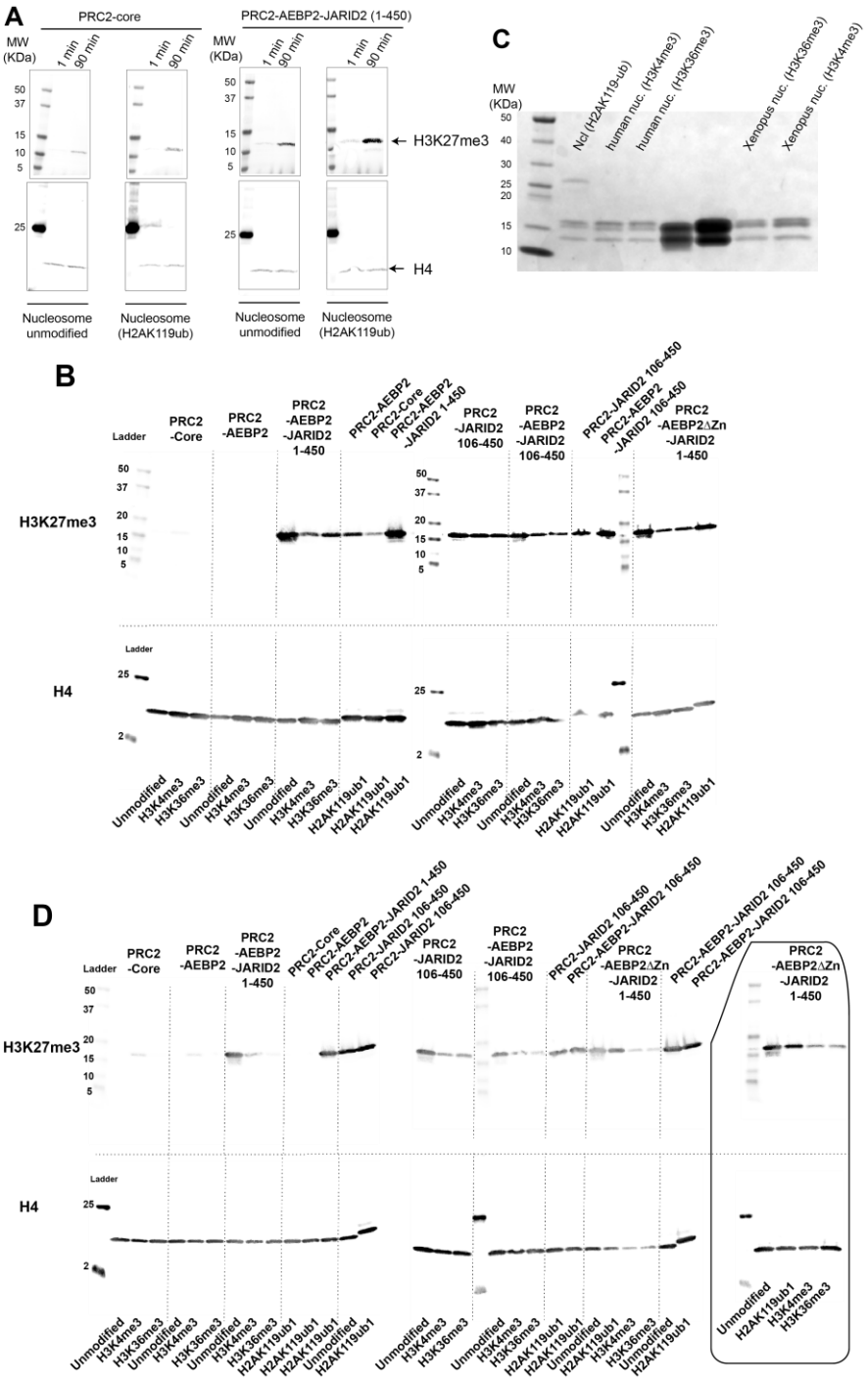

Fig. S9. (A) Raw images of the western blot activity assay for PRC2-core and PRC2-AEBP2-JARID2 (aa 1-450) with either unmodified nucleosome or H2AK119ub containing nucleosome. Top panel shows Cy5 fluorescence images for H3K27me3 while bottom panel shows Cy3 fluorescence image for H4. (B) Raw images of the western blot activity assay for PRC2-core, PRC2-A, PRC2-$J_{106-450}$, PRC2-AJ_{1-450}, and PRC2-AΔZnJ_{1-450} with Xenopus nucleosomes

unmodified, H3K4me3-containing, H3K36me3-containing, and H2AK119ub1-containing. Top panel shows Cy5 fluorescence images for H3K27me3 while bottom panel show Cy3 fluorescence images for H4. (C) Coomassie stained 4-12% Tris-Glycine SDS-PAGE gels of the different nucleosomes used, showing the presence of all four histones. (D) Raw images of the western blot activity assay for PRC2-core, PRC2-A, PRC2-$J_{106-450}$, PRC2-AJ_{1-450}, and PRC2-$A\Delta ZnJ_{1-450}$ with human unmodified, H3K4me3-containing, H3K36me3-containing, and H2AK119ub1-containing nucleosomes. Top panel shows Cy5 fluorescence images for H3K27me3 while bottom panel show Cy3 fluorescence images for H4. Repetition of activity assay for PRC2-JARID2 106-450 and PRC2-AEBP2-JARID2 106-450 with Xenopus unmodified and Xenopus H2AK119ub1-containing nucleosomes are included again due to the observed defective loading controls in (B) for H2AK119ub1-containing nucleosome for these PRC2 complexes. The repetition of the activity assay of PRC2-$A\Delta ZnJ_{1-450}$ with human nucleosomes due to lower loading (seen in (D)) is shown in the inset (black box).

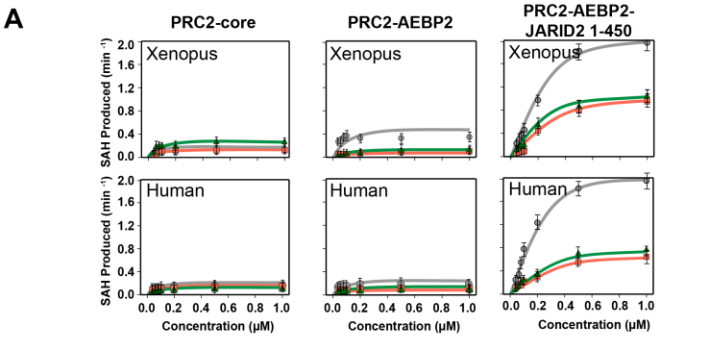

C

		PRC2-Core			PRC2-AEBP2			PRC2-AEBP2-JARID2 1-450		
		Unmodified	H3K4me3	H3K36me3	Unmodified	H3K4me3	H3K36me3	Unmodified	H3K4me3	H3K36me3
Xenopus	Vmax	0.131 ± 0.03	0.154 ± 0.04	0.275 ± 0.04	0.373 ± 0.04	0.113 ± 0.01	0.187 ± 0.04	2.11 ± 0.23	0.832 ± 0.19	0.914 ± 0.23
	Km (μM)	0.039 ± 0.02	0.082 ± 0.02	0.041 ± 0.02	0.047 ± 0.02	0.158 ± 0.04	0.271 ± 0.08	0.108 ± 0.08	0.231 ± 0.07	0.209 ± 0.14
Human	Vmax	0.141 ± 0.02	0.108 ± 0.01	0.100 ± 0.01	0.171 ± 0.004	0.074 ± 0.01	0.076 ± 0.01	2.17 ± 0.24	0.51 ± 0.06	0.65 ± 0.07
	Km (μM)	0.026 ± 0.003	0.032 ± 0.004	0.076 ± 0.011	0.017 ± 0.002	0.019 ± 0.01	0.031 ± 0.013	0.131 ± 0.06	0.248 ± 0.04	0.248 ± 0.04

D

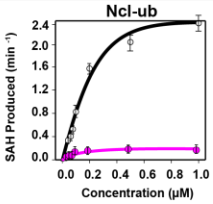

		PRC2-Core		PRC2-AEBP2-JARID2 1-450	
		Unmodified	Ncl-ub	Unmodified	Ncl-ub
Xenopus	Vmax	0.131 ± 0.03	0.142 ± 0.06	2.11 ± 0.23	2.41 ± 0.14
	Km (μM)	0.039 ± 0.02	0.044 ± 0.05	0.108 ± 0.08	0.103 ± 0.08

Fig. S10. (A) Comparison of HMTase activity of PRC2 on Xenopus versus Human H3K4/K36me3 containing nucleosomes. Kinetic assays showing initial rates of four different PRC2 complexes with increasing amounts of either Xenopus nucleosomes either unmodified (grey) or containing H3K4me3 (orange) or H3K36me3 (green). (Bottom) As top row, but using Human nucleosomes. (B) Bar graph showing end point assays for cumulative H3K27me/me2/me3 activity for different PRC2 complexes on human nucleosomes: unmodified (grey), H3K4me3-containing (orange), H3K36me3-containing (green), and H2AK119ub1-containing (Pink). (C) Summary of the Michaelis-Menten kinetic parameters V_{max}, K_M obtained by fitting the curves in panel (A). (D) HMTase activity of PRC2-core (magenta) and PRC2-AEBP2-JARID2 1-450 (black) on H2AK119ub1-containing nucleosome. Summary of the Michaelis-Menten kinetic parameters V_{max}, and K_M obtained by fitting the curves.

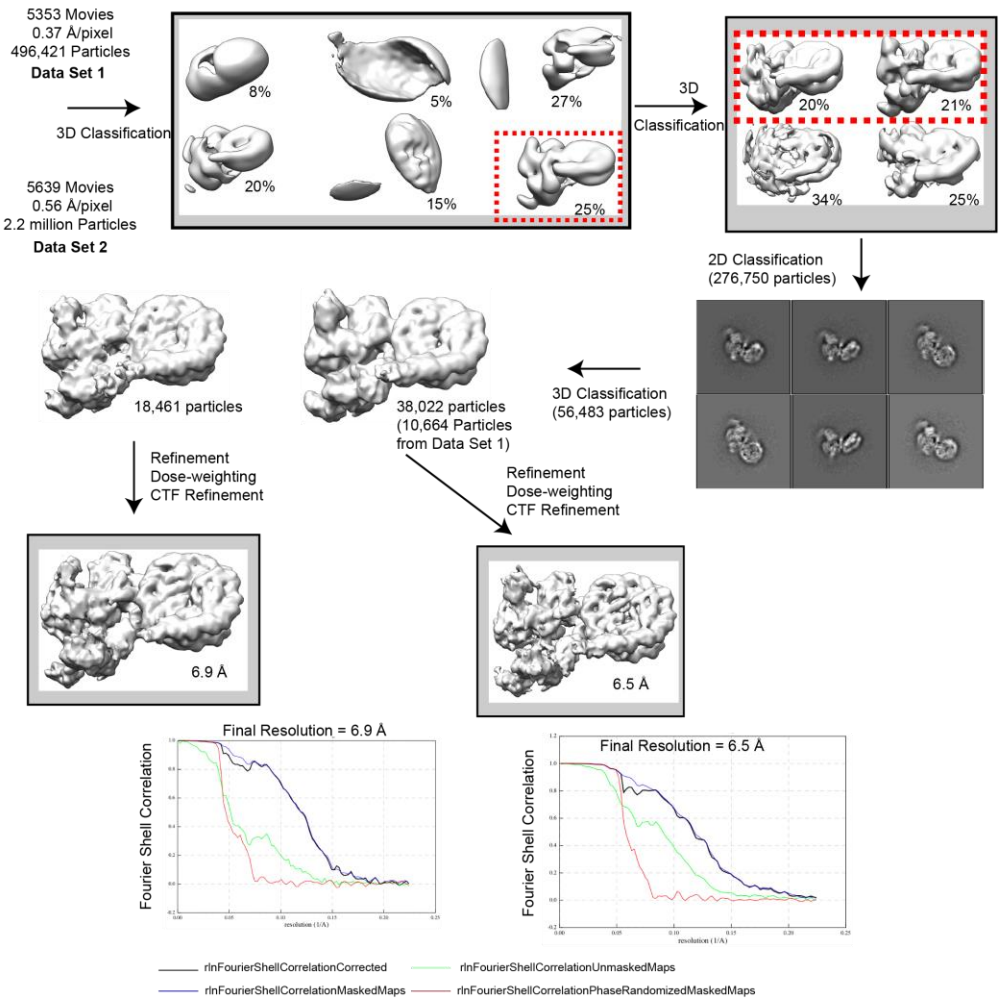

Fig. S11. Processing workflow for the combined data sets of PRC2-AEBP2-JARID2 (aa 1-450) bound to human H3K4me3-containing mono-nucleosome collected on a Titan Krios with a Gatan K3 camera.

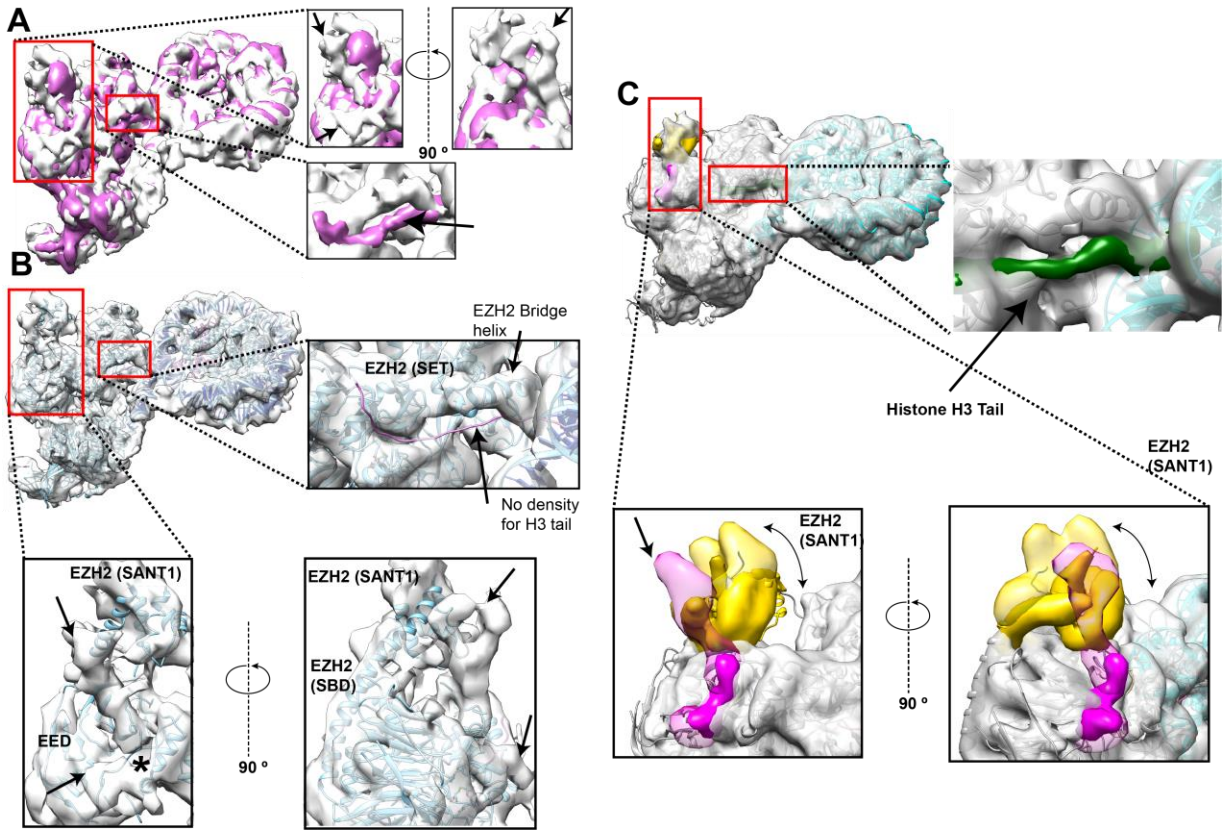

Fig. S12. (A) Overlay of cryo-EM density maps for PRC2-AJ$_{1\text{-}450}$ bound to human H3K4me3 (light grey: state without density for H3 tail) and to Xenopus Ncl-ub (purple) nucleosomes. Both maps are lowpass filtered to 8 Å for comparison. At the displayed threshold (=0.03) the density for ubiquitin, the AEBP2 zinc-fingers and the JARID2 UIM are not visible in the Ncl-ub map. The red boxes highlight regions of notable differences and are shown in close-up views on the right. (Top inset) Orthogonal close-up views of the EED, EZH2 (SANT1, SBD) region and JARID2 K116me3 binding region, with differences in the PRC2 bound to H3K4me3-containing nucleosome indicated by black arrows. (Bottom inset) Close-up view of the EZH2 (SET) catalytic domain showing that the density for H3 tail is observed in the PRC2-Ncl-ub reconstruction but it is absent in that for PRC2 bound to the H3K4me3-containing nucleosome. (B) The atomic model for PRC2 and nucleosome (cyan) from this study was fitted into the cryo-EM reconstruction of PRC2-AJ$_{1\text{-}450}$ bound to Human H3K4me3 nucleosome (light grey) after removing ubiquitin, the JARID2 (UIM) and the AEBP2 zinc-fingers. The docked model shows that the overall geometry of interaction between PRC2 and the two types of nucleosome is the same. Flexible fitting was used in iMODFIT(*59*) to account for the differences in the EZH2 (SANT1, SBD) region. The SBD of EZH2 adopts a straight conformation and repositions the SANT1 domain, as also observed in one of the two active states in our earlier study of the PRC2-AEBP2-JARID2 structure without nucleosome, and in our previous structure of PRC2-AEBP2 bound to a dinucleosome(*22*, *23*). (Top inset) Close-up view of the EZH2 (SET) domain showing the absence of density for the histone H3 tail in the catalytic region. (Bottom inset) Close-up view of the EED, EZH2 (SANT1, SBD) region and JARID2 K116me3 binding region showing unaccounted density (indicated by black arrow) observed in PRC2 bound to H3K4me3-containing nucleosome. The unaccounted density is near the region on EED where JARID2 K116me3 or H3K27me3 bind, but it occupies a

larger volume and does not appear to overlap significantly with the JARID2 K116me3 segment (indicated by *) observed in the PRC2-AJ_{1-450} bound to Ncl-ub. (C) (Top) Cryo-EM density map for PRC2-AJ_{1-450} bound to human H3K4me3 (light grey) containing the histone H3 tail engaged in the EZH2 (SET) catalytic site. Inset shows an enlarged view, with the density for the histone H3 tail segmented in green. (Bottom) Comparison of the differences in the SANT1 (yellow) and the allosteric binding site region on EED (magenta) between the two states. The differences in position of SANT1 are indicated by the curved arrow, while the extra density observed bound to the allosteric region of EED in the state without H3 tail is shown in magenta (marked by solid arrow).

Table S1. Cryo-EM data collection, refinement and validation statistics for the different data sets for the different data sets - #1: PRC2-AEBP2-JARID2 1-450+Ncl-ub, #2: PRC2-AEBP2-JARID2 1-450+Ncl-ub; #3-PRC2-AEBP2-JARID2 1-450+Ncl; #4:PRC2-AEBP2+Ncl; #5:PRC2-AEBP2-JARID2 106-450+Ncl-ub; #6: PRC2-AEBP2-JARID2 1-450+human Ncl (H3K4me3). Only the combined map from dataset #1 and #2 were used for model building.

Data Collection	Dataset #1	Dataset #2	Dataset #3	Dataset #4	Dataset #5	Dataset #6
Microscope	Krios	Krios	Arctica	Krios	Arctica	Krios
Voltage (kV)	300	300	200	300	200	300
Detector	K3	K2	K3	K3	K3	K3
Energy Filter (slit width eV)	GIF Quantum (20 eV)	GIF Quantum (20 eV)		GIF Quantum (20 eV)		GIF Quantum (20 eV)
Pixel Size (Å)	0.37	0.575	0.45	0.575	0.57	0.37 & 0.56
Defocus Range (μm)	-1 to -2.5	-1 to -2.5	-1 to -2.5	-1 to -2.5	-1 to -2.5	-0.6 to -2.5
Movies	10750	10354	1066	7900	3095	5353 & 5639
Exposure Rate ($e^-/Å^2$)	50	50	50	50	50	50
Reconstruction						
Software	RELION	RELION	RELION	RELION	RELION	RELION
Particles (final)	168601	64632	20578	72655	55740	56483
Box Size (pixels)	384	384	384	360	384	384
Accuracy Rotations (º)	0.84	1.43	3.71	2.7	3.5	1.3
Accuracy Translations (Å)	0.5	1.1	3.9	2.1	3.3	0.98
Map Resolution (Å)	3.5	4.2	18	5.7	15	6.9
Map Sharpening B-factor ($Å^2$)	-60	-100		-142		
Coordinate Refinement						
Software	PHENIX					
Map CC	0.84					
Resolution Cutoff (Å)	3.5					
Box Size (Å)	169x207x171					
$FSC_{model\text{-}vs\text{-}map}$ = 0.5 (Å)	3.6					
Model						
Number of Atoms	27916					
Protein	2831					
Nucleic Acid	314					
B-factors overall	100					
Protein	100					
Nucleic acid	100					
R.m.s deviations						
Bond Length (Å)	0.005					
Bond angles (º)	0.61					
Validation						
Molprobity score	2.4					
Clashscore	8.57					
Rotamer outliers (%)	0.0					
C_β deviations (%)	0					
Ramachandran						
Favored (%)	87.2					
Allowed (%)	12.8					
Outliers (%)	0.0					
CaBLAM outliers (%)	4.17					
EMRinger Score	1.78					

Movie 1 - Cryo-EM density map (3.5 Å overall resolution) of PRC2-AJ$_{1-450}$ bound to Ncl-Ub, segmented with colors corresponding to the different proteins and/or domains of PRC2 and the nucleosome (as in Fig. 1), with the corresponding atomic model, shown in ribbon, for the whole assembly (same color scheme).

References and Notes

1. A. P. Bracken, K. Helin, Polycomb group proteins: Navigators of lineage pathways led astray in cancer. *Nat. Rev. Cancer* **9**, 773–784 (2009). doi:10.1038/nrc2736 Medline

2. B. Schuettengruber, G. Cavalli, Recruitment of polycomb group complexes and their role in the dynamic regulation of cell fate choice. *Development* **136**, 3531–3542 (2009). doi:10.1242/dev.033902 Medline

3. L. Di Croce, K. Helin, Transcriptional regulation by Polycomb group proteins. *Nat. Struct. Mol. Biol.* **20**, 1147–1155 (2013). doi:10.1038/nsmb.2669 Medline

4. R. Margueron, D. Reinberg, The Polycomb complex PRC2 and its mark in life. *Nature* **469**, 343–349 (2011). doi:10.1038/nature09784 Medline

5. R. Cao, L. Wang, H. Wang, L. Xia, H. Erdjument-Bromage, P. Tempst, R. S. Jones, Y. Zhang, Role of histone H3 lysine 27 methylation in Polycomb-group silencing. *Science* **298**, 1039–1043 (2002). doi:10.1126/science.1076997 Medline

6. S. Hauri, F. Comoglio, M. Seimiya, M. Gerstung, T. Glatter, K. Hansen, R. Aebersold, R. Paro, M. Gstaiger, C. Beisel, A High-Density Map for Navigating the Human Polycomb Complexome. *Cell Rep.* **17**, 583–595 (2016). doi:10.1016/j.celrep.2016.08.096 Medline

7. S. Cooper, A. Grijzenhout, E. Underwood, K. Ancelin, T. Zhang, T. B. Nesterova, B. Anil-Kirmizitas, A. Bassett, S. M. Kooistra, K. Agger, K. Helin, E. Heard, N. Brockdorff, Jarid2 binds mono-ubiquitylated H2A lysine 119 to mediate crosstalk between Polycomb complexes PRC1 and PRC2. *Nat. Commun.* **7**, 13661 (2016). doi:10.1038/ncomms13661 Medline

8. S. Kaneko, R. Bonasio, R. Saldaña-Meyer, T. Yoshida, J. Son, K. Nishino, A. Umezawa, D. Reinberg, Interactions between JARID2 and noncoding RNAs regulate PRC2 recruitment to chromatin. *Mol. Cell* **53**, 290–300 (2014). doi:10.1016/j.molcel.2013.11.012 Medline

9. X. Wang, R. D. Paucek, A. R. Gooding, Z. Z. Brown, E. J. Ge, T. W. Muir, T. R. Cech, Molecular analysis of PRC2 recruitment to DNA in chromatin and its inhibition by RNA. *Nat. Struct. Mol. Biol.* **24**, 1028–1038 (2017). doi:10.1038/nsmb.3487 Medline

10. N. P. Blackledge, A. M. Farcas, T. Kondo, H. W. King, J. F. McGouran, L. L. P. Hanssen, S. Ito, S. Cooper, K. Kondo, Y. Koseki, T. Ishikura, H. K. Long, T. W. Sheahan, N. Brockdorff, B. M. Kessler, H. Koseki, R. J. Klose, Variant PRC1 complex-dependent H2A ubiquitylation drives PRC2 recruitment and polycomb domain formation. *Cell* **157**, 1445–1459 (2014). doi:10.1016/j.cell.2014.05.004 Medline

11. N. P. Blackledge, N. A. Fursova, J. R. Kelley, M. K. Huseyin, A. Feldmann, R. J. Klose, PRC1 Catalytic Activity Is Central to Polycomb System Function. *Mol. Cell* **77**, 857–874.e9 (2020). doi:10.1016/j.molcel.2019.12.001 Medline

12. S. Tamburri, E. Lavarone, D. Fernández-Pérez, E. Conway, M. Zanotti, D. Manganaro, D. Pasini, Histone H2AK119 Mono-Ubiquitination Is Essential for Polycomb-Mediated Transcriptional Repression. *Mol. Cell* **77**, 840–856.e5 (2020). doi:10.1016/j.molcel.2019.11.021 Medline

13. R. Kalb, S. Latwiel, H. I. Baymaz, P. W. T. C. Jansen, C. W. Müller, M. Vermeulen, J. Müller, Histone H2A monoubiquitination promotes histone H3 methylation in Polycomb repression. *Nat. Struct. Mol. Biol.* **21**, 569–571 (2014). doi:10.1038/nsmb.2833 Medline

14. S. J. Whitcomb, B. Fierz, R. K. McGinty, M. Holt, T. Ito, T. W. Muir, C. D. Allis, Histone monoubiquitylation position determines specificity and direction of enzymatic cross-talk with histone methyltransferases Dot1L and PRC2. *J. Biol. Chem.* **287**, 23718–23725 (2012). doi:10.1074/jbc.M112.361824 Medline

15. E. M. Mendenhall, R. P. Koche, T. Truong, V. W. Zhou, B. Issac, A. S. Chi, M. Ku, B. E. Bernstein, GC-rich sequence elements recruit PRC2 in mammalian ES cells. *PLOS Genet.* **6**, e1001244 (2010). doi:10.1371/journal.pgen.1001244 Medline

16. T. S. Mikkelsen, M. Ku, D. B. Jaffe, B. Issac, E. Lieberman, G. Giannoukos, P. Alvarez, W. Brockman, T.-K. Kim, R. P. Koche, W. Lee, E. Mendenhall, A. O'Donovan, A. Presser, C. Russ, X. Xie, A. Meissner, M. Wernig, R. Jaenisch, C. Nusbaum, E. S. Lander, B. E. Bernstein, Genome-wide maps of chromatin state in pluripotent and lineage-committed cells. *Nature* **448**, 553–560 (2007). doi:10.1038/nature06008 Medline

17. A. Grijzenhout, J. Godwin, H. Koseki, M. R. Gdula, D. Szumska, J. F. McGouran, S. Bhattacharya, B. M. Kessler, N. Brockdorff, S. Cooper, Functional analysis of AEBP2, a PRC2 Polycomb protein, reveals a Trithorax phenotype in embryonic development and in ESCs. *Development* **143**, 2716–2723 (2016). doi:10.1242/dev.123935 Medline

18. G. Li, R. Margueron, M. Ku, P. Chambon, B. E. Bernstein, D. Reinberg, Jarid2 and PRC2, partners in regulating gene expression. *Genes Dev.* **24**, 368–380 (2010). doi:10.1101/gad.1886410 Medline

19. A. P. Aiden, M. N. Rivera, E. Rheinbay, M. Ku, E. J. Coffman, T. T. Truong, S. O. Vargas, E. S. Lander, D. A. Haber, B. E. Bernstein, Wilms tumor chromatin profiles highlight stem cell properties and a renal developmental network. *Cell Stem Cell* **6**, 591–602 (2010). doi:10.1016/j.stem.2010.03.016 Medline

20. F. W. Schmitges, A. B. Prusty, M. Faty, A. Stützer, G. M. Lingaraju, J. Aiwazian, R. Sack, D. Hess, L. Li, S. Zhou, R. D. Bunker, U. Wirth, T. Bouwmeester, A. Bauer, N. Ly-Hartig, K. Zhao, H. Chan, J. Gu, H. Gut, W. Fischle, J. Müller, N. H. Thomä, Histone methylation by PRC2 is inhibited by active chromatin marks. *Mol. Cell* **42**, 330–341 (2011). doi:10.1016/j.molcel.2011.03.025 Medline

21. W. Yuan, M. Xu, C. Huang, N. Liu, S. Chen, B. Zhu, H3K36 methylation antagonizes PRC2-mediated H3K27 methylation. *J. Biol. Chem.* **286**, 7983–7989 (2011). doi:10.1074/jbc.M110.194027 Medline

22. V. Kasinath, M. Faini, S. Poepsel, D. Reif, X. A. Feng, G. Stjepanovic, R. Aebersold, E. Nogales, Structures of human PRC2 with its cofactors AEBP2 and JARID2. *Science* **359**, 940–944 (2018). doi:10.1126/science.aar5700 Medline

23. S. Poepsel, V. Kasinath, E. Nogales, Cryo-EM structures of PRC2 simultaneously engaged with two functionally distinct nucleosomes. *Nat. Struct. Mol. Biol.* **25**, 154–162 (2018). doi:10.1038/s41594-018-0023-y Medline

24. C.-H. Lee, M. Holder, D. Grau, R. Saldaña-Meyer, J.-R. Yu, R. A. Ganai, J. Zhang, M. Wang, G. LeRoy, M.-W. Dobenecker, D. Reinberg, K.-J. Armache, Distinct Stimulatory

Mechanisms Regulate the Catalytic Activity of Polycomb Repressive Complex 2. *Mol. Cell* **70**, 435–448.e5 (2018). doi:10.1016/j.molcel.2018.03.019 Medline

25. C.-H. Lee, J.-R. Yu, J. Granat, R. Saldaña-Meyer, J. Andrade, G. LeRoy, Y. Jin, P. Lund, J. M. Stafford, B. A. Garcia, B. Ueberheide, D. Reinberg, Automethylation of PRC2 promotes H3K27 methylation and is impaired in H3K27M pediatric glioma. *Genes Dev.* **33**, 1428–1440 (2019). doi:10.1101/gad.328773.119 Medline

26. X. Wang, Y. Long, R. D. Paucek, A. R. Gooding, T. Lee, R. M. Burdorf, T. R. Cech, Regulation of histone methylation by automethylation of PRC2. *Genes Dev.* **33**, 1416–1427 (2019). doi:10.1101/gad.328849.119 Medline

27. L. Jiao, X. Liu, Structural basis of histone H3K27 trimethylation by an active polycomb repressive complex 2. *Science* **350**, aac4383 (2015). doi:10.1126/science.aac4383 Medline

28. N. Justin, Y. Zhang, C. Tarricone, S. R. Martin, S. Chen, E. Underwood, V. De Marco, L. F. Haire, P. A. Walker, D. Reinberg, J. R. Wilson, S. J. Gamblin, Structural basis of oncogenic histone H3K27M inhibition of human polycomb repressive complex 2. *Nat. Commun.* **7**, 11316 (2016). doi:10.1038/ncomms11316 Medline

29. M. T. Morgan, M. Haj-Yahya, A. E. Ringel, P. Bandi, A. Brik, C. Wolberger, Structural basis for histone H2B deubiquitination by the SAGA DUB module. *Science* **351**, 725–728 (2016). doi:10.1126/science.aac5681 Medline

30. H. Wang, C. Dienemann, A. Stützer, H. Urlaub, A. C. M. Cheung, P. Cramer, Structure of the transcription coactivator SAGA. *Nature* **577**, 717–720 (2020). doi:10.1038/s41586-020-1933-5 Medline

31. J. Son, S. S. Shen, R. Margueron, D. Reinberg, Nucleosome-binding activities within JARID2 and EZH1 regulate the function of PRC2 on chromatin. *Genes Dev.* **27**, 2663–2677 (2013). doi:10.1101/gad.225888.113 Medline

32. E. J. Ge, K. S. Jani, K. L. Diehl, M. M. Müller, T. W. Muir, Nucleation and propagation of heterochromatin by the histone methyltransferase PRC2: Geometric constraints and impact of the regulatory subunit JARID2. *J. Am. Chem. Soc.* **141**, 15029–15039 (2019). doi:10.1021/jacs.9b02321

33. M. D. Simon, F. Chu, L. R. Racki, C. C. de la Cruz, A. L. Burlingame, B. Panning, G. J. Narlikar, K. M. Shokat, The site-specific installation of methyl-lysine analogs into recombinant histones. *Cell* **128**, 1003–1012 (2007). doi:10.1016/j.cell.2006.12.041 Medline

34. S. Kaneko, J. Son, S. S. Shen, D. Reinberg, R. Bonasio, PRC2 binds active promoters and contacts nascent RNAs in embryonic stem cells. *Nat. Struct. Mol. Biol.* **20**, 1258–1264 (2013). doi:10.1038/nsmb.2700 Medline

35. Q. Zhang, N. J. McKenzie, R. Warneford-Thomson, E. H. Gail, S. F. Flanigan, B. M. Owen, R. Lauman, V. Levina, B. A. Garcia, R. B. Schittenhelm, R. Bonasio, C. Davidovich, RNA exploits an exposed regulatory site to inhibit the enzymatic activity of PRC2. *Nat. Struct. Mol. Biol.* **26**, 237–247 (2019). doi:10.1038/s41594-019-0197-y Medline

36. S. K. Kia, M. M. Gorski, S. Giannakopoulos, C. P. Verrijzer, SWI/SNF mediates polycomb eviction and epigenetic reprogramming of the INK4b-ARF-INK4a locus. *Mol. Cell. Biol.* **28**, 3457–3464 (2008). doi:10.1128/MCB.02019-07 Medline

37. K. Finogenova, J. Bonnet, S. Poepsel, I. B. Schäfer, K. Finkl, K. Schmid, C. Litz, M. Strauss, C. Benda, J. Müller, Structural basis for PRC2 decoding of active histone methylation marks H3K36me2/3. *eLife* **9**, e61964 (2020). doi:10.7554/eLife.61964

38. B. E. Bernstein, T. S. Mikkelsen, X. Xie, M. Kamal, D. J. Huebert, J. Cuff, B. Fry, A. Meissner, M. Wernig, K. Plath, R. Jaenisch, A. Wagschal, R. Feil, S. L. Schreiber, E. S. Lander, A bivalent chromatin structure marks key developmental genes in embryonic stem cells. *Cell* **125**, 315–326 (2006). doi:10.1016/j.cell.2006.02.041 Medline

39. S. D. Gradia, J. P. Ishida, M.-S. Tsai, C. Jeans, J. A. Tainer, J. O. Fuss, MacroBac: New Technologies for Robust and Efficient Large-Scale Production of Recombinant Multiprotein Complexes. *Methods Enzymol.* **592**, 1–26 (2017). doi:10.1016/bs.mie.2017.03.008 Medline

40. P. N. Dyer, R. S. Edayathumangalam, C. L. White, Y. Bao, S. Chakravarthy, U. M. Muthurajan, K. Luger, Reconstitution of nucleosome core particles from recombinant histones and DNA. *Methods Enzymol.* **375**, 23–44 (2003). doi:10.1016/S0076-6879(03)75002-2 Medline

41. L. Long, M. Furgason, T. Yao, Generation of nonhydrolyzable ubiquitin-histone mimics. *Methods* **70**, 134–138 (2014). doi:10.1016/j.ymeth.2014.07.006 Medline

42. K. Zhang, Gctf: Real-time CTF determination and correction. *J. Struct. Biol.* **193**, 1–12 (2016). doi:10.1016/j.jsb.2015.11.003 Medline

43. S. Q. Zheng, E. Palovcak, J.-P. Armache, K. A. Verba, Y. Cheng, D. A. Agard, MotionCor2: Anisotropic correction of beam-induced motion for improved cryo-electron microscopy. *Nat. Methods* **14**, 331–332 (2017). doi:10.1038/nmeth.4193 Medline

44. S. H. Scheres, RELION: Implementation of a Bayesian approach to cryo-EM structure determination. *J. Struct. Biol.* **180**, 519–530 (2012). doi:10.1016/j.jsb.2012.09.006 Medline

45. B. G. Han, Z. Watson, H. Kang, A. Pulk, K. H. Downing, J. Cate, R. M. Glaeser, Long shelf-life streptavidin support-films suitable for electron microscopy of biological macromolecules. *J. Struct. Biol.* **195**, 238–244 (2016). doi:10.1016/j.jsb.2016.06.009 Medline

46. T. Bepler, A. Morin, M. Rapp, J. Brasch, L. Shapiro, A. J. Noble, B. Berger, Positive-unlabeled convolutional neural networks for particle picking in cryo-electron micrographs. *Nat. Methods* **16**, 1153–1160 (2019). doi:10.1038/s41592-019-0575-8 Medline

47. G. Tang, L. Peng, P. R. Baldwin, D. S. Mann, W. Jiang, I. Rees, S. J. Ludtke, EMAN2: An extensible image processing suite for electron microscopy. *J. Struct. Biol.* **157**, 38–46 (2007). doi:10.1016/j.jsb.2006.05.009 Medline

48. P. Emsley, K. Cowtan, *Coot*: Model-building tools for molecular graphics. *Acta Cryst.* **D60**, 2126–2132 (2004). doi:10.1107/S0907444904019158 Medline

49. Y. Sato, A. Yoshikawa, H. Mimura, M. Yamashita, A. Yamagata, S. Fukai, Structural basis for specific recognition of Lys 63-linked polyubiquitin chains by tandem UIMs of RAP80. *EMBO J.* **28**, 2461–2468 (2009). doi:10.1038/emboj.2009.160 Medline

50. A. Sun, F. Li, Z. Liu, Y. Jiang, J. Zhang, J. Wu, Y. Shi, Structural and biochemical insights into human zinc finger protein AEBP2 reveals interactions with RBBP4. *Protein Cell* **9**, 738–742 (2018). doi:10.1007/s13238-017-0483-6 Medline

51. F. Long, A. A. Vagin, P. Young, G. N. Murshudov, *BALBES*: A molecular-replacement pipeline. *Acta Cryst.* **D64**, 125–132 (2008). doi:10.1107/S0907444907050172 Medline

52. E. J. Worden, X. Zhang, C. Wolberger, Structural basis for COMPASS recognition of an H2B-ubiquitinated nucleosome. *eLife* **9**, e53199 (2020). doi:10.7554/eLife.53199 Medline

53. S. Vijay-Kumar, C. E. Bugg, W. J. Cook, Structure of ubiquitin refined at 1.8 Å resolution. *J. Mol. Biol.* **194**, 531–544 (1987). doi:10.1016/0022-2836(87)90679-6 Medline

54. P. D. Adams, R. W. Grosse-Kunstleve, L.-W. Hung, T. R. Ioerger, A. J. McCoy, N. W. Moriarty, R. J. Read, J. C. Sacchettini, N. K. Sauter, T. C. Terwilliger, *PHENIX*: Building new software for automated crystallographic structure determination. *Acta Cryst.* **D58**, 1948–1954 (2002). doi:10.1107/S0907444902016657 Medline

55. A. Leitner, T. Walzthoeni, R. Aebersold, Lysine-specific chemical cross-linking of protein complexes and identification of cross-linking sites using LC-MS/MS and the xQuest/xProphet software pipeline. *Nat. Protoc.* **9**, 120–137 (2014). doi:10.1038/nprot.2013.168 Medline

56. J. Cox, M. Mann, MaxQuant enables high peptide identification rates, individualized p.p.b.-range mass accuracies and proteome-wide protein quantification. *Nat. Biotechnol.* **26**, 1367–1372 (2008). doi:10.1038/nbt.1511 Medline

57. J. G. Tate, S. Bamford, H. C. Jubb, Z. Sondka, D. M. Beare, N. Bindal, H. Boutselakis, C. G. Cole, C. Creatore, E. Dawson, P. Fish, B. Harsha, C. Hathaway, S. C. Jupe, C. Y. Kok, K. Noble, L. Ponting, C. C. Ramshaw, C. E. Rye, H. E. Speedy, R. Stefancsik, S. L. Thompson, S. Wang, S. Ward, P. J. Campbell, S. A. Forbes, COSMIC: The Catalogue Of Somatic Mutations In Cancer. *Nucleic Acids Res.* **47**, D941–D947 (2019). doi:10.1093/nar/gky1015 Medline

58. A. A. Rizzo, P. E. Salerno, I. Bezsonova, D. M. Korzhnev, NMR Structure of the Human Rad18 Zinc Finger in Complex with Ubiquitin Defines a Class of UBZ Domains in Proteins Linked to the DNA Damage Response. *Biochem.* **53**, 5895–5906 (2014). doi:10.1021/bi500823h Medline

59. J. R. Lopéz-Blanco, P. Chacón, iMODFIT: Efficient and robust flexible fitting based on vibrational analysis in internal coordinates. *J. Struct. Biol.* **184**, 261–270 (2013). doi:10.1016/j.jsb.2013.08.010 Medline